Heavy-Ion-Induced Displacement Damage Effects on WO_x ECRAM

Matthew J. Marinella[®], Senior Member, IEEE, Christopher H. Bennett[®], Member, IEEE, Brian Zutter, Max Siath, Matthew Spear[®], Member, IEEE, Gyorgy Vizkelethy[®], Member, IEEE, T. Patrick Xiao[®], Member, IEEE, Elliot Fuller[®], David Hughart[®], Member, IEEE, Sapan Agarwal[®], Member, IEEE, Yiyang Li, and A. Alec Talin[®]

Abstract—Electrochemical random-access memory (ECRAM) is an emerging nonvolatile memory device which is promising for analog in-memory computing applications. Displacement damage in WO_{3-x} ECRAM was experimentally characterized for the first time using a 1 MeV Au beam. At moderate levels of displacement damage (below fluence of $\sim 10^{11}$ cm⁻²), metal oxide ECRAM does not exhibit significant change, demonstrating the suitability of ECRAM for applications such as spaceborne computing. At high fluences ($> 10^{11}$ cm⁻²), where high concentrations of oxygen vacancies are created, channel conductivity was found to increase linearly with increasing vacancy concentration. A model of vacancy concentration versus conductivity allows the extraction of the mobility and initial doping concentration.

Index Terms—Electrochemical random-access memory (ECRAM), heavy ion irradiation, mobility, neuromorphic computing, nonvolatile memory, vacancies.

I. INTRODUCTION

ELECTROCHEMICAL random-access memory (ECRAM) is a family of emerging nonvolatile memory devices that shows significant promise for applications that require a stable analog resistance that can be precisely tuned over many orders of magnitude [1], [2]. ECRAM, also referred to as electrochemical ion synapses (EIS) devices, are of particular interest for implementing efficient neural network processing using an architecture known as analog in-memory

Manuscript received 1 January 2024; accepted 3 January 2024. Date of publication 19 February 2024; date of current version 18 April 2024. This work was supported in part by the Laboratory-Directed Research and Development (LDRD) Program; and in part by the National Technology and Engineering Solutions of Sandia, LLC with the U.S. Department of Energy (DOE) under Contract DE-NA0003525. The work of Matthew J. Marinella and A. Alec Talin was supported by the DOE Office of Science Research Program for Microelectronics Codesign (sponsored by ASCR, BES, HEP, NP, and FES) through the Abisko Project, PM Robinson Pino (ASCR). The work of Yiyang Li was supported in part by the National Science Foundation under Grant CCF-2235316. (Corresponding author: Matthew J. Marinella.)

Matthew J. Marinella, Max Siath, and Matthew Spear are with the Electrical, Computer and Energy Engineering, Arizona State University, Tempe, AZ 85281 USA (e-mail: m@asu.edu).

Christopher H. Bennett, Gyorgy Vizkelethy, T. Patrick Xiao, and David Hughart are with Sandia National Laboratories, Albuquerque, NM 87185 USA (e-mail: cbennet@sandia.gov).

Brian Zutter, Elliot Fuller, and Sapan Agarwal are with Sandia National Laboratories, Livermore, CA 94550 USA (e-mail: btzutte@sandia.gov).

Yiyang Li is with the Materials Science Department, University of Michigan, Ann Arbor, MI 48109 USA (e-mail: yiyangli@umich.edu).

A. Alec Talin is with Sandia National Laboratories, Livermore, CA 94550 USA (e-mail: aatalin@sandia.gov).

Color versions of one or more figures in this article are available at https://doi.org/10.1109/TNS.2024.3360409.

Digital Object Identifier 10.1109/TNS.2024.3360409

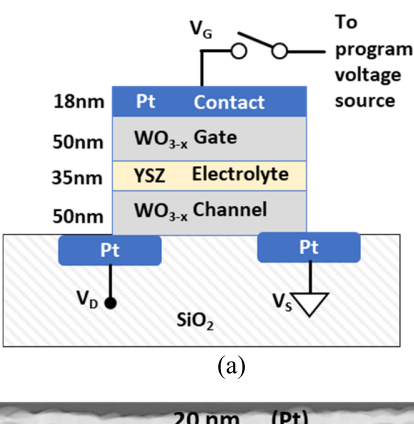
computing (AIMC) [3], [4]. They are able to meet key AIMC requirements [5] including low "read" current, "write" linearity, low "write" asymmetry, low switching energy, high endurance and excellent retention due to the three-terminal structure and bulk switching mechanism [6]. In this architecture, by combining an analog weight with digital CMOS support circuitry, it is possible to process neural networks with performance per watt from 10× to 100× beyond the standard state of the art [7]. Ultimately, AIMC could enable new capabilities such as real-time in-sensor data processing, for spaceborne applications such as satellites. Hence, there is significant interest in technologies like ECRAM which can serve as "synapses" for these AIMC processors.

Alternative AIMC synapse devices such as metal oxide resistive memory (ReRAM, also referred to as memristors) suffer from high nonlinearity, asymmetry, and write variability, making it difficult to achieve highly accurate training [8]. These issues are likely due to the inherently stochastic process of filamentary switching in ReRAM. Conversely, ECRAM switching is a bulk effect and hence does not suffer this stochasticity. Furthermore, phase change memories often show significant resistance drift at high resistance states [9], which can affect the accuracy of inference over long periods of time. ECRAM synapses have demonstrated significant improvement in all of these regards, spurring significant research toward their use in AIMC systems [1], [2], [3].

Early ECRAM devices demonstrated were based on Li-Ion battery materials, such as lithium cobalt oxide (LCO) [1]. However, the use of Li-based materials with CMOS poses integration challenges [6]. More recent variants of ECRAM, sometimes referred to as "bulk resistive memory" use fabcompatible metal oxides, including TiO_x [10] and WO_{3-x} [11] as a channel material. A comprehensive list of materials used for ECRAM is provided in [3]. Metal oxide ECRAM have exhibited excellent retention even at high temperatures, and hence are a strong candidate for use as long-term synapses in AIMC systems for use in harsh environments, such as space. However, although it has been well established that ReRAM using similar materials is typically resilient to moderate levels of displacement damage [12], [13], there have been no radiation effects studies to date on metal oxide ECRAM.

The WO_{3-x} device structure used in this study is illustrated in Fig. 1(a). Although the structure has a "gate," "source," and "drain" terminal, the operation is different from a MOSFET.

0018-9499 © 2024 IEEE. Personal use is permitted, but republication/redistribution requires IEEE permission. See https://www.ieee.org/publications/rights/index.html for more information.



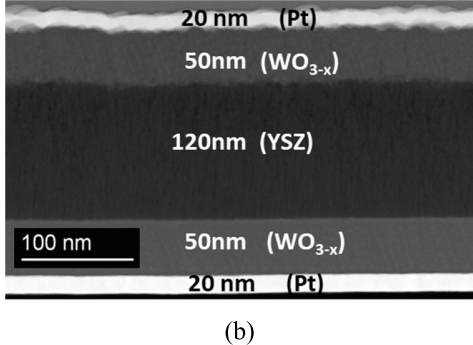


Fig. 1. (a) WO_{3-x} ECRAM device structure. The gate is connected to a voltage source during programming mode and disconnected in read or inference mode. (b) SEM image of the ECRAM stack.

Specifically, the gate modulates the bulk oxygen vacancy concentration (V_O^2) in the channel, which act as an n-type dopants thus modulating the free carrier concentration, and hence the conductivity of the channel. The WO_{3-x} ECRAM has "true" retention [11], meaning that whether the gate is grounded or floating, when a small bias is applied to the drain with the source grounded, a linear current–voltage behavior is measured. Once programmed, this resistance can be used to represent a weight (or synapse) when performing inference on AIMC accelerators.

The WO_{3-x} ECRAM has two modes of operation, program (or training) and read (or inference). Programming requires biasing the gate [V_G in Fig. 1(a)] at an elevated temperature (typically ~120 °C). In the case of a negative gate bias of approximately -2 V, oxygen vacancies are removed from the channel. Oxygen vacancies act as n-type dopants and hence this increases the resistance of the channel. Conversely, a positive bias of approximately +2 V will add vacancies to the channel and decrease resistance. Programming typically requires hundreds of seconds [11]. In read, or inference mode, the gate is typically disconnected (floating) within the array to ensure the conductivity state is not electrically altered. This mode would be achieved through the use a transistor or select device with a high ON–OFF ratio [14].

Similar to metal oxide ReRAM, the WO_{3-x} ECRAM is expected to be more tolerant to ionizing radiation than traditional charge-based nonvolatile memories like flash and charge-trapping memories, due to the lack of a direct charge interaction [12]. It is also expected to be tolerant to moderate levels of displacement damage in a similar manner to

TABLE I
APPROXIMATE ECRAM DIMENSIONS

Channel Width	420 μm	
Channel Length	540 μm	
Gate Width	140 μm	
Drain Length	110 μm	
Source Length	110 μm	

filamentary ReRAM, and at high levels, the conductivity is expected to drop, similar to ReRAM [15]. However, unlike filamentary ReRAM, ECRAM is a bulk switching device, and hence, the conductivity should be related directly to the vacancy concentration induced in the channel. Understanding and quantifying the relationship between oxygen vacancies in the channel and the channel conductance can help illustrate ECRAM device physics.

Hence, there are two key reasons to study displacement damage in WO_{3-x} : First, as this device is a leading candidate for spaceborne AIMC neural accelerators, we want to confirm that it is tolerant to displacement damage. Even minor changes in channel conductance due to radiation can significantly affect deep neural network inference accuracy [16]. Second, we would like to better understand channel conductance in bulk devices. Both topics are novel in the literature for metal-oxide ECRAM.

II. EXPERIMENTAL DETAILS

Lateral WO_{3-x} ECRAM was fabricated as follows. A 20 nm of Pt was sputtered on a Si substrate with 500 nm of thermal SiO₂ using an AJA Orion-8 Sputter system through a shadow mask to define the bottom Pt contacts for the source and drain. The DC sputtering used a power of 100 W, a process gas of 3 mtorr Ar, and a 2-in Pt target. Next, a trilayer of WO_{3-X} , followed by yttria-stabilized zirconia (YSZ) and ending with WO_{3-x} was consecutively sputtered with a second shadow mask consisting of a 0.5×1.7 mm cutout. Each 50 nm WO_{3-X} layer was sputtered using DC sputtering on a 3-in W target with a power of 100 W. The process gas was a 1:1 ratio of Ar:O₂ at a pressure of 3 mtorr. The 120 nm YSZ layer was sputtered using RF sputtering on a 3-in YSZ target with a process gas of 3 mtorr of Ar and a power of 150 W. The vacuum was not broken during the sputtering. The top layer of Pt was sputtered using DC sputtering in the same way. All shadow masks were made from a 0.13 mm thick stainlesssteel sheet and cut using a CO₂ laser by Stencils Unlimited. All sputtering was done at room temperature; no additional annealing was conducted. The baseline pressure of the sputter system was below 10⁻⁶ torr. A scanning electron microscope image of the final stack is given in Fig. 1(b).

An optical micrograph of the ECRAM is illustrated prior to radiation in Fig. 2(a) with key dimensions indicated in Table I. The channel length was \sim 420 μ m, and width was \sim 540 μ m. The dimensions in Table I are approximate, as measured from the microscope, and vary slightly from the as-drawn features due to the nature of the shadow mask process.

Before wire bonding, the two ECRAM devices to be irradiated were preprogrammed to two-channel resistances. Devices

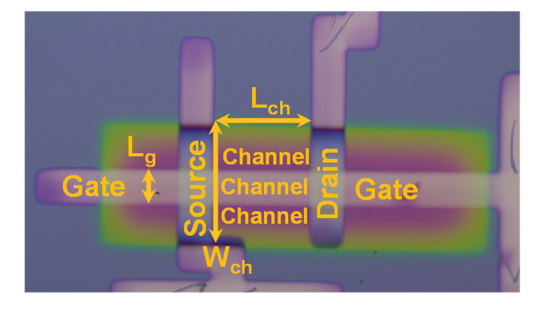


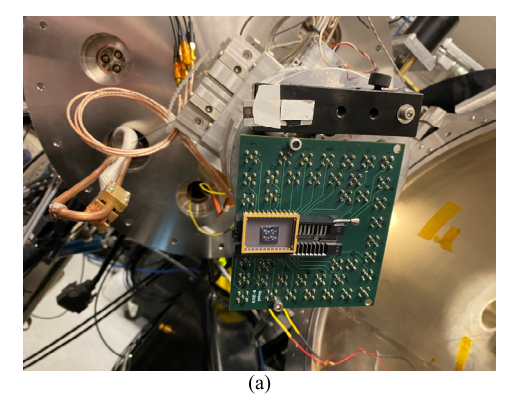
Fig. 2. Microscope image of the lateral WO_x ECRAM prior to irradiation.

were packaged in a metal dual inline package (DIP) with only the source and drain wire bonded. The reason the gate was not wire bonded was twofold: first, the gate is sensitive to ESD effects, which had the potential to destroy the device prior to the experiment. Second, the purpose of this initial experiment was to measure the device in a read-mode or inference-mode state, where the gate terminal in an array would be placed in a high-impedance configuration. Hence, disconnecting the gate best replicates this realistic condition. Devices were initially programmed to resistances of 2.82 M Ω (Device 1) and 3.40 M Ω (Device 2) at a temperature of 120 °C. These resistances were intentionally set higher than in [11] because devices in the higher resistance states were expected to be more susceptible to change due to ion damage than those in the lower resistance states. Two devices on the same substrate and in the same package were measured over the course of two days, where Device 1 was irradiated on the first day and Device 2 on the second day.

Displacement damage experiments took place at Sandia's Ion Beam Laboratory using a 6 MV High Voltage Engineering tandem van de Graaff accelerator. The DIP was mounted on a board in the end station vacuum chamber [Fig. 3(a)]. Au ions were chosen for this displacement damage study due to their high nonionizing energy loss, and the ability to focus the beam and create significant damage in the key layers of a specific device. A 1 MeV Au beam was chosen, with flux of 1.5×10^{13} – 1.5×10^{14} ions/cm²/s, depending on the shot. The beam was focused on an approximately 1×1 mm spot, allowing us to isolate and apply radiation to a single device.

Stopping range of ions in matter (SRIM) [17] calculations were used to model the ion behavior and guide the energy and fluence choice for the stack illustrated in Fig. 1(b). The WO_{x-3} channel is expected to be the most important layer since displacement damage caused by heavy ions in this region will directly affect the device's conductivity. Channel stoichiometry is assumed to be WO_3 for the calculation, with a density of 7.4×10^{22} atoms/cm³ in the channel. The resulting oxygen vacancy concentration versus distance across the WO_{3-x} channel (vertically) is plotted for the range of ion fluences use in this experiment in Fig. 4. It was found that 1000 keV Au confined the damage to the device layers.

Channel resistance was measured in the chamber prior to and between shots using an Agilent B1505A semiconductor parameter analyzer without removing the device from the vacuum. Measurements were performed within 5 min following



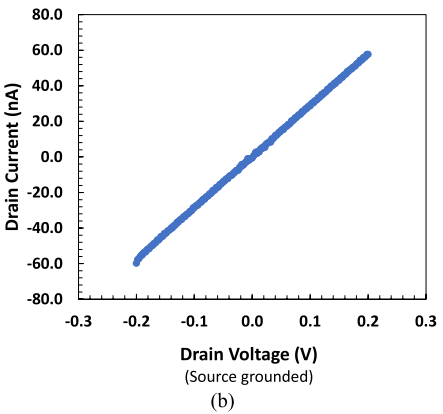


Fig. 3. (a) Wire-bonded ECRAM die mounted in Sandia IBL's vacuum chamber. (b) Typical prerad current–voltage curve for the lateral WO_x ECRAM device used in this work.

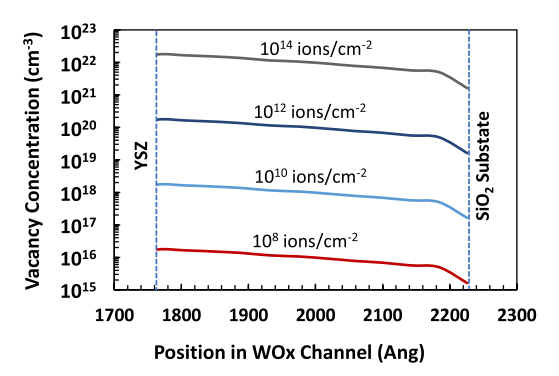


Fig. 4. Vacancy concentration in the channel as a function of 1 MeV Au ion fluence as calculated by SRIM.

the end of each shot. The resistance was obtained by grounding the source terminal and sweeping the drain between -0.2 and +0.2 V [Fig. 3(b)]. This measurement was performed three times and averaged for each value. Both packaged devices were measured on all runs to ensure that the unirradiated device was not affected by neighboring radiation.

III. RESULTS AND DISCUSSION

The measured resistance following each exposure to progressively increasing fluences for the two ECRAM devices is plotted in Fig. 5. Each resistance point is the mean of three measurements, with a standard measurement error of <0.5% in all cases. As observed in Fig. 5, the measured change in resistance is relatively unaffected through a fluence of $\sim 10^{11}$ ion/cm² for both devices, corresponding to

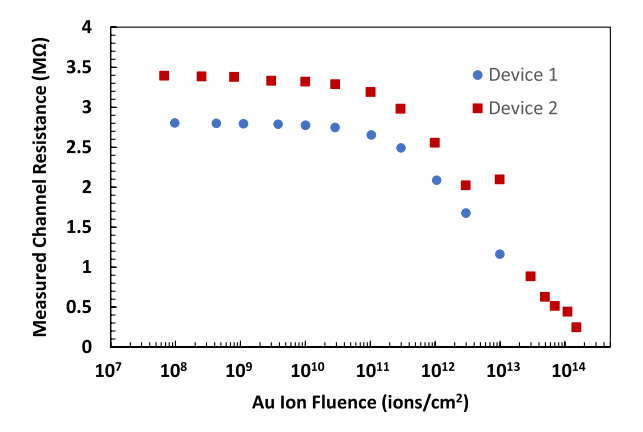


Fig. 5. ECRAM channel resistance versus 1 MeV Au ion fluence.

a vacancy concentration of approximately 8×10^{18} oxygen vacancies/cm³ in the channel. While interpreting these results, note that the W atoms account for about 80% of the atomic weight in the channel, whereas the O is about 20%; hence, there are significantly more O displacements than W displacements. An oxygen vacancy concentration of 10^{19} cm⁻³ corresponds to $\sim 2 \times 10^{-4}$ displacements per atom (DPA), meaning that approximately 2 in every $10\,000$ oxygen atoms are displaced before a significant conductivity increase is observed. For reference, in the channel of this ECRAM, a single 1 MeV Au ion creates displacement damage approximately equivalent to that caused by 10^5 10 MeV protons. Hence, these results suggest sustained resilience in a typical natural space environment [18].

Above 10^{11} ions/cm², both device resistances drop (channel conductances increase) monotonically following each other for the remainder of the shots. There is one exception, Device 2 following a fluence of $\sim 10^{13}$ ions/cm². This anomalous point was included for completeness but appears to be most likely an error, possibly indicating a problem with the shot.

The two devices on the same substrate served as each other's controls. During the first day of the experiment when the beam was focused only on Device 1; Device 2 was out of range of the beam and served as a control. During this period when Device 2 was out of the beam range and Device 1 was under irradiation, the resistance was stable, exhibiting a slight shift between 3.47 and 3.40 M Ω , which might be attributed to the device being in a vacuum environment. Similarly, during the second day of the experiment when Device 2 was irradiated, Device 1 served as a control. In this case, only a very slight drift was observed in the resistance of Device 1, 1.40 and 1.38 M Ω during the entire period that Device 2 was being irradiated.

The range of 10^{11} – 10^{14} ions/cm² was investigated to elucidate the role of vacancy creation in conductivity of WO_{3-x} ECRAM and enable estimation of electron mobility in the WO_{3-x} channel as discussed below. The conductivity versus vacancy concentration is plotted for the entire range for both devices in Fig. 6.

Device 2 conductivity continued to increase through the exposure of 1.5×10^{14} ion/cm², which resulted in an additional vacancy concentration of 1.2×10^{22} cm⁻³, and a final

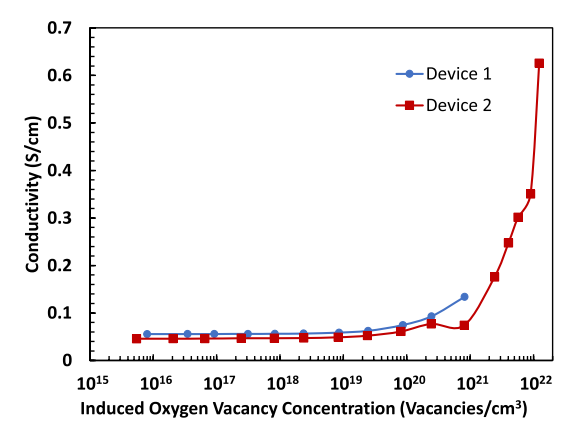


Fig. 6. ECRAM conductivity versus induced oxygen vacancy concentration in the WO_{3-x} channel.

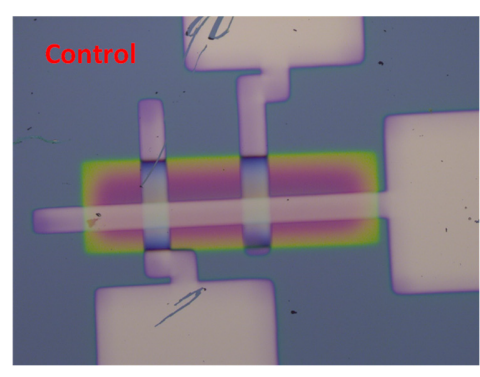
DPA of >0.2. This means that more than 20% of the oxygen atoms in the channel will have experienced a displacement effect, and hence, it was surprising that conductivity continued to increase at this level. Interestingly, this suggests that heavy ion induced vacancy creation is a method to finely tune the conductivity of a metal oxide ECRAM channel. However, this method would need to be calibrated in such a way that damage to the gate and electrolyte regions do not reduce device endurance.

Device 1 and Device 2 had resistances of 1.161 M Ω and 249 k Ω immediately after receiving their final fluences 10^{13} and 1.5×10^{14} ions/cm², respectively, indicating that neither device catastrophically failed. Given Device 2 had a DPA of \sim 0.2 following the exposure, it was expected that physical damage may have occurred. For this reason, the device was optically inspected following the exposure for visual signs of damage. However, as seen in Fig. 7, there are no apparent visual indications of damage due to the ion beam.

Although a formal annealing study was not performed, it was observed that the resistance of Device 1 drifted from 1.161 M Ω following the final post-irradiation measurement on the first day to 1.398 M Ω at the beginning of the second day. This recovery of 237 k Ω toward the preradiation (higher) resistance is well above the standard measurement error for this resistance range (5.0 k Ω). During this same period, Device 2, which had not yet received radiation, but had experienced identical conditions otherwise only drifted from 3.397 to 3.402 M Ω , which is within the measurement error for this resistance range (9.6 k Ω). Hence, it appears that an annealing occurred such that Device 1 recovered a portion of the resistance degradation over the course of \sim 12 h at room temperature. This may represent the annihilation of a portion of the radiation-induced oxygen vacancies. However, the exact mechanism of this recovery remains unclear, and may be an interesting topic for future studies.

A. Mobility Analysis

It is possible to use the relationship between conductivity in the WO_{3-x} channel versus vacancy concentration to quantify electron mobility. First, it should be noted that displacement damage will generate significant oxygen vacancies in the YSZ



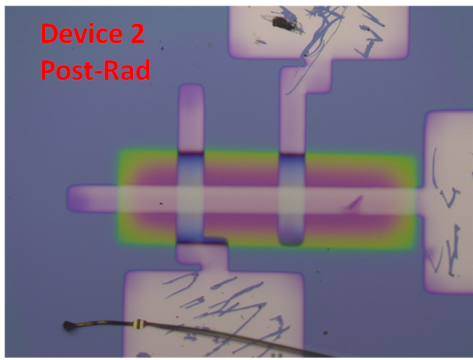


Fig. 7. Optical micrograph of the control device compared to Device 2 following a fluence of 1×10^{14} 1 MeV Au ions. There is no visual abnormality following the high level of damage.

and WO_{3-x} gate layers. However, we assume that YSZ retains its insulating nature, which confines the observed channel conductivity modulation to the WO_{3-x} channel layer. If we also assume that in WO_{3-x} each oxygen vacancy is acting as an ionized dopant V_0^{2+} , providing two free conduction electrons [19], and assume that the mobility only depends on the concentration of free electrons, we can use the relationship

$$\mu_n = \frac{\sigma_{\text{ch}}}{qn} = \frac{\sigma_{\text{ch}}}{2q\left(N_{v0} + N_{v_{\text{ion}}}\right)} \tag{1}$$

where μ_n is the electron mobility in the WO₃ channel, $\sigma_{\rm ch}$ is the channel conductivity, n is the free electron concentration, N_{v0} is the initial, as fabricated ionized vacancy concentration, and N_{vion} is the ionized vacancy concentration caused by the ion beam. This equation assumes all vacancies are ionized. Rearranging (1) provides the relationship between channel conductivity as a function of induced ions as

$$\sigma_{\rm ch}(N_{\nu_{\rm ion}}) = 2q\,\mu_n N_{\nu_{\rm ion}} + 2q\,\mu_n N_{\nu 0}. \tag{2}$$

This is now expressed as a standard linear relationship between σ_{ch} and $N_{v_{\rm ion}}$. Hence, a plot of $\sigma_{\rm ch}$ versus $N_{v_{\rm ion}}$ will have a slope of $2q\,\mu_n$ and intercept by $2q\,\mu_n N_{v0}$. This suggests the mobility and initial doping concentration can easily be found from a least squares linear fit to a plot of $\sigma_{\rm ch}$ versus $N_{v_{\rm ion}}$, with the slope of this plot providing the mobility as

$$\mu_n = \frac{\text{slope}}{2q N_{v_{\text{ion}}}}.$$

The intercept can be used to provide the initial ion concentration, as

$$N_{v0} = \frac{\text{intercept}}{2q\mu_n}.$$

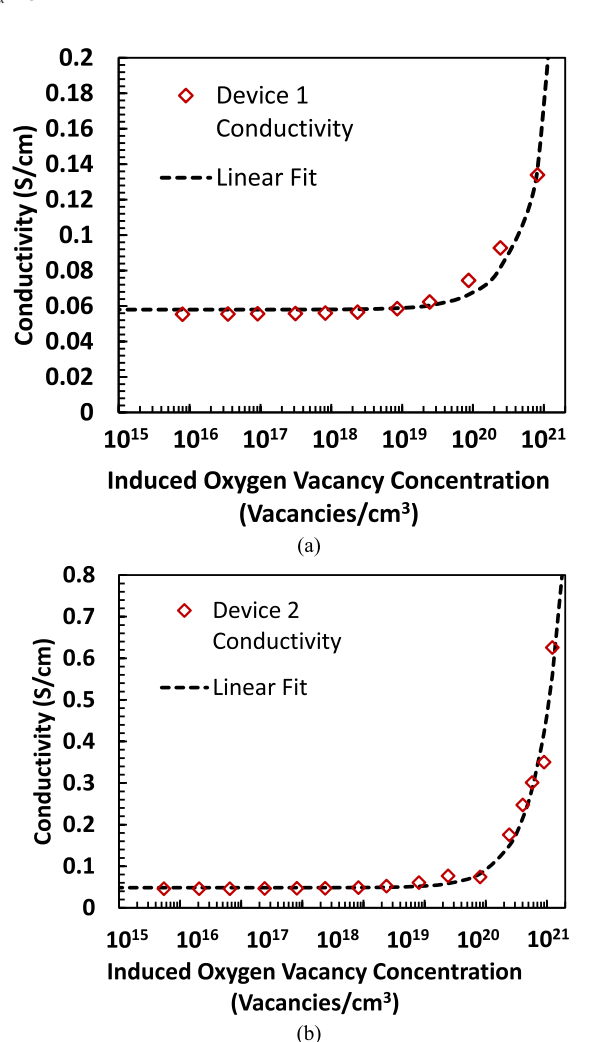


Fig. 8. Conductivity versus vacancy concentration for (a) Device 1 and (b) Device 2 in the range where a linear fit was possible.

TABLE II
EXTRACTED MOBILITY AND INITIAL DOPING CONCENTRATION

Sample	Mobility (μ_n)	Initial Doping Concentration (N_{v0})
Device 1	3.1x10 ⁻⁴ cm ² /Vs	5.9x10 ²⁰ cm ⁻³
Device 2	$1.3x10^{-4} \text{ cm}^2/\text{Vs}$	1.2x10 ²¹ cm ⁻³

Fig. 8 plots $\sigma_{\rm ch}$ versus $N_{\nu_{\rm ion}}$ and the least squares linear fits, which were used to solve for the two mobilities and initial doping concentrations provided in Table II. The model provided an excellent fit to Device 2 [Fig. 8(b)] and reasonable fit to Device 1 [Fig. 8(a)]. It is possible that the extended levels of vacancy concentrations over a wide range of conductivity was responsible for the improved fit in Device 2.

Although relatively little electron mobility data exists for amorphous WO₃, the values in Table II are clearly lower than the previous report of 0.3 cm²/V-s [20]. This is not surprising since even in solids referred to as "amorphous" there may be different degrees of short-range order, including nanocrystalline domains. Damage from the ion beam may have decreased the short-range order during the experiment,

increasing scattering and ultimately reducing the mobility for a given electron concentration. It is also possible that the vacancies induced by the ion beam are not all ionized. In this case, the estimated mobility would be increased by a factor of N_v/N_v^+ where N_v is the total number of vacancies and N_v^+ is the total number of ionized vacancies at room temperature. This represents the inverse of the fraction of vacancies that are ionized at room temperature.

IV. CONCLUSION

Heavy ion-induced displacement damage has been characterized for the first time in metal oxide ECRAM. No significant change in channel conductivity was observed at ion fluences below $\sim\!10^{11}$ ion/cm², corresponding to a DPA of 1.5×10^{-4} , suggesting resilience to prolonged exposure to space environments. At higher fluences, conductivity decreased due to oxygen vacancy creation. A model was developed to quantify conductivity change as a function of induced vacancies and estimate the electron mobility in the channel. This provided evidence that the increase in electron concentration due to vacancy creation was likely the cause of increased conductivity.

ACKNOWLEDGMENT

The employee owns all right, titles, and interests in and to the article and is solely responsible for its contents. The United States Government retains and the publisher, by accepting the article for publication, acknowledges that the United States Government retains a non-exclusive, paidup, irrevocable, worldwide license to publish or reproduce the published form of this article or allow others to do so, for United States Government purposes. The DOE will provide public access to these results of federally sponsored research in accordance with the DOE Public Access Plan https://www.energy.gov/downloads/doe-public-access-plan.

REFERENCES

- [1] E. J. Fuller et al., "Li-ion synaptic transistor for low power analog computing," *Adv. Mater.*, vol. 29, no. 4, Jan. 2017, Art. no. 1604310.
- [2] M. Onen, J. Li, B. Yildiz, and J. A. D. Alamo, "Dynamics of PSG-based nanosecond protonic programmable resistors for analog deep learning," in *IEDM Tech. Dig.*, Dec. 2022 Dec. 2022, pp. 1–4, doi: 10.1109/IEDM45625.2022.10019365.
- [3] M. Huang, M. Schwacke, M. Onen, J. del Alamo, J. Li, and B. Yildiz, "Electrochemical ionic synapses: Progress and perspectives," Adv. Mater., vol. 35, no. 37, Sep. 2023, Art. no. 2205169, doi: 10.1002/adma.202205169.

- [4] E. J. Fuller et al., "Redox transistors for neuromorphic computing," IBM J. Res. Develop., vol. 63, no. 6, pp. 1–9, Nov. 2019, doi: 10.1147/JRD.2019.2942285.
- [5] S. Agarwal et al., "Resistive memory device requirements for a neural algorithm accelerator," in *Proc. Int. Joint Conf. Neural Netw. (IJCNN)*, 2016, pp. 929–938, doi: 10.1109/IJCNN.2016.7727298.
- [6] A. A. Talin, Y. Li, D. A. Robinson, E. J. Fuller, and S. Kumar, "ECRAM materials, devices, circuits and architectures: A perspective," *Adv. Mater.*, vol. 35, no. 37, Sep. 2023, Art. no. 2204771, doi: 10.1002/adma.202204771.
- [7] T. P. Xiao, C. H. Bennett, B. Feinberg, S. Agarwal, and M. J. Marinella, "Analog architectures for neural network acceleration based on non-volatile memory," *Appl. Phys. Rev.*, vol. 7, no. 3, Sep. 2020, Art. no. 031301.
- [8] M. J. Marinella et al., "Multiscale co-design analysis of energy, latency, area, and accuracy of a ReRAM analog neural training accelerator," *IEEE J. Emerg. Sel. Topics Circuits Syst.*, vol. 8, no. 1, pp. 86–101, Mar. 2018, doi: 10.1109/JETCAS.2018.2796379.
- [9] D. Ielmini, S. Lavizzari, D. Sharma, and A. L. Lacaita, "Physical interpretation, modeling and impact on phase change memory (PCM) reliability of resistance drift due to chalcogenide structural relaxation," in *IEDM Tech. Dig.*, Dec. 2007, pp. 939–942, doi: 10.1109/IEDM.2007. 4419107.
- [10] Y. Li et al., "Filament-free bulk resistive memory enables deterministic analogue switching," Adv. Mater., vol. 32, no. 45, Nov. 2020, Art. no. 2003984, doi: 10.1002/adma.202003984.
- [11] D. S. Kim et al., "Nonvolatile electrochemical random-access memory under short circuit," *Adv. Electron. Mater.*, vol. 9, no. 1, Jan. 2023, Art. no. 2200958, doi: 10.1002/aelm.202200958.
- [12] D. R. Hughart et al., "A comparison of the radiation response of TaO_x and TiO_2 memristors," *IEEE Trans. Nucl. Sci.*, vol. 60, no. 6, pp. 4512–4519, Dec. 2013, doi: 10.1109/TNS.2013.2285516.
- [13] Y. Gonzalez-Velo, H. J. Barnaby, and M. N. Kozicki, "Review of radiation effects on ReRAM devices and technology," *Semicond. Sci. Technol.*, vol. 32, no. 8, Jul. 2017, Art. no. 083002, doi: 10.1088/1361-6641/aa6124.
- [14] E. J. Fuller et al., "Parallel programming of an ionic floating-gate memory array for scalable neuromorphic computing," *Science*, vol. 364, no. 6440, pp. 570–574, May 2019, doi: 10.1126/science.aaw5581.
- [15] M. J. Marinella et al., "Initial assessment of the effects of radiation on the electrical characteristics of TaO_x memristive memories," *IEEE Trans. Nucl. Sci.*, vol. 59, no. 6, pp. 2987–2994, Dec. 2012, doi: 10.1109/TNS.2012.2224377.
- [16] T. P. Xiao et al., "Ionizing radiation effects in SONOS-based neuromorphic inference accelerators," *IEEE Trans. Nucl. Sci.*, vol. 68, no. 5, pp. 762–769, May 2021, doi: 10.1109/TNS.2021.3058548.
- [17] J. F. Ziegler, M. D. Ziegler, and J. P. Biersack, "SRIM—The stopping and range of ions in matter (2010)," *Nucl. Instrum. Methods Phys. Res. Sect. B, Beam Interact. Mater. At.*, vol. 268, nos. 11–12, pp. 1818–1823, Jun. 2010, doi: 10.1016/j.nimb.2010.02.091.
- [18] M. A. Xapsos, C. Stauffer, T. Jordan, J. L. Barth, and R. A. Mewaldt, "Model for cumulative solar heavy ion energy and linear energy transfer spectra," *IEEE Trans. Nucl. Sci.*, vol. 54, no. 6, pp. 1985–1989, Dec. 2007, doi: 10.1109/TNS.2007.910850.
- [19] M. Gillet, C. Lemire, E. Gillet, and K. Aguir, "The role of surface oxygen vacancies upon WO3 conductivity," *Surf. Sci.*, vols. 532–535, pp. 519–525, Jun. 2003, doi: 10.1016/s0039-6028(03)00477-1.
- [20] S. Yamada, T. Nakamura, Y. Hiruta, K. Urabe, and M. Kitao, "Electron diffusion in amorphous tungsten oxide films," *Jpn. J. Appl. Phys.*, vol. 22, no. 5, pp. 789–793, May 1983, doi: 10.1143/jjap.22.789.